



1

## **Applying dynamical systems techniques to real ocean drifters**

2

Irina I. Rypina<sup>1</sup>, Timothy Getscher<sup>2</sup>, Lawrence Pratt<sup>1</sup>, and Tamay Ozgokmen<sup>3</sup>

3

<sup>1</sup>Woods Hole Oceanographic Institution, 266 Woods Hole rd., Woods Hole, MA 02540

4

<sup>2</sup>US Navy

5

<sup>3</sup>Rosenstiel School of Marine and Atmospheric Science, U. of Miami, 4600 Rickenbacker

6

Causeway, Miami, FL 33149

7

Corresponding author: Irina I. Rypina, [irypina@whoi.edu](mailto:irypina@whoi.edu)

8

9

10

11

12

13

14

15

16

17

18



19 **Abstract**

20 This paper presents the first comprehensive comparison of several different dynamical-systems-  
21 based measures of stirring and Lagrangian coherence, computed from real ocean drifters. Seven  
22 commonly used methods (finite-time Lyapunov exponent, trajectory path length, trajectory  
23 correlation dimension, trajectory encounter volume, Lagrangian-averaged vorticity deviation,  
24 dilation, and spectral clustering) were applied to 135 surface drifters in the Gulf of Mexico in  
25 order to map out the dominant Lagrangian coherent structures. Among the detected structures  
26 were regions of hyperbolic nature resembling stable manifolds from classical examples,  
27 divergent and convergent zones, and groups of drifters that moved more coherently and stayed  
28 closer together than the rest of the drifters. Many methods highlighted the same structures, but  
29 there were differences too. Overall, 5 out of 7 methods provided useful information about the  
30 geometry of transport within the domain spanned by the drifters.

31

32

33

34

35

36

37

38



39 **Significance statement**

40 This paper applies different Lagrangian methods to identify Lagrangian Coherent Structures  
41 based on trajectories of 135 ocean surface drifters from the massive drifter release in the Gulf of  
42 Mexico. To our knowledge, this is the first comprehensive comparison of the performance of  
43 several different dynamical systems techniques with applications to real ocean drifters.

44

45

46

47

48

49

50

51

52

53

54

55

56



57 **1. Introduction**

58 Techniques from the dynamical systems theory can be used to study transport and exchange  
59 processes in oceanic flows (Haller, 2015; Samelson and Wiggins, 2006; Balasuriya et al., 2019;  
60 Hadjighasem et al., 2017; Filippi et al., 2021; Rypina et al., 2010 and others). In general, they  
61 aim to identify the key regions of the flow with qualitatively different Lagrangian behavior  
62 and/or to identify boundaries between them. The term Lagrangian Coherent Structures or LCS  
63 (Haller and Juan, 2000) has been adopted to refer to both such regions themselves and to their  
64 boundaries. Because different methods use different definitions of “different” and “similar,” they  
65 generally yield different LCS (Balasuriya et al. 2019; Rypina et al. 2011; 2018; Hadjighasem et  
66 al., 2017).

67 Being Lagrangian in nature, most LCS detection methods start with the release of a set of  
68 particles or drifters within the domain of interest, and then observation of their trajectories as the  
69 particles are advected by the flow. Obtaining such trajectory datasets is straightforward in  
70 applications where the velocity fields are known from either models or observations, and this is  
71 exactly the settings in which the dynamical system approach has been used in the past. However,  
72 applying the same techniques to real ocean drifters has been a challenge simply because the  
73 drifters are rarely released in a manner that adequately spans the domain of interest.

74 On April 21<sup>st</sup> 2018, 135 near-surface CARTHE drifters were released nearly simultaneously in a  
75 roughly 10 km by 11 km domain in the northern Gulf of Mexico as part of the Submesoscale  
76 Processes and Lagrangian Analysis on the Shelf (SPLASH) experiment (Laxague et al., 2018;  
77 Solodoch et al., 2020; Lund et al., 2020). The release pattern was a nearly regular, rectangular,  
78 11 x 12 grid with roughly 1 km average spacing between neighboring drifters. The release was



79 done using 7 boats and took less than 2 hours. The drifters then transmitted their positions every  
80 5 min during the subsequent 5 days. The deployment positions and the resulting drifter  
81 trajectories are shown in Fig. 1. Such aggressive release strategy is not typical for oceanographic  
82 applications due to high costs of vessels and manpower. However, it allowed populating the  
83 domain with drifters in a manner most suitable for the dynamical systems applications. Thus, this  
84 dataset provided a unique and long-awaited opportunity to try applying the dynamical systems  
85 techniques to real, rather than simulated, ocean drifters and to identify the real, rather than  
86 simulated, ocean LCS.

87 In this paper, seven commonly used dynamical systems techniques were applied to the real  
88 drifter dataset from the SPLASH experiment: FTLEs, trajectory path length, trajectory  
89 correlation dimension, encounter volume, Lagrangian-averaged vorticity deviation, dilation, and  
90 spectral clustering. The resulting real ocean LCS were mapped and described and, when  
91 possible, parallels were made between these observed structures and their more classical  
92 counterparts from text-book analytic or numeric examples. The seven techniques were also inter-  
93 compared to each other and the similarities/differences were discussed. Our choice of the seven  
94 techniques is by no means all-inclusive and was inspired by Hadjighasem et al. (2017) who  
95 compared a similar selection of the dynamical systems methods (plus a few more and minus the  
96 encounter volume method) in the context of analytical and numerically-generated flows.

## 97 **2. Methods**

98 We start with a brief review of the 7 dynamical systems techniques that we will use.

### 99 **a) FTLEs**



100 One of the most commonly used LCS detection techniques is based upon FTLEs (Haller and  
101 Yuan, 2000; Shadden et al., 2005). FTLE is the largest exponential separation rate between a  
102 trajectory and its closest neighbors in any direction. Maximizing ridges of FTLE fields can be  
103 used as proxies for stable (or unstable for backward-time trajectories) manifolds of hyperbolic  
104 trajectories in time-varying fluid flows (with the additional requirement that the fastest  
105 separation occurs in the direction normal to the ridge and is caused by the hyperbolic straining  
106 rather than shear). Regions with small FTLEs are indicative of slow separation rates between  
107 neighboring trajectories and often correspond to eddy cores, although for eddies with a non-  
108 solid-body rotating regime, azimuthal shear produces spiraling structures within the core region  
109 instead of the uniformly low FTLEs. Maps of FTLEs are very visual, and the computation of  
110 FTLEs is straightforward, computationally inexpensive, and robust with respect to noise, which  
111 makes FTLEs one of the most popular methods in oceanographic studies of transport and  
112 mixing. Importantly, FTLEs are also frame-independent and thus give consistent results in any  
113 translating or rotating reference frame (Haller 2005; 2015).

114 For flows where the velocity field is known from either models or observations, FTLEs ( $\lambda$ ) can  
115 be estimated by releasing dense regularly-spaced orthogonal grids of simulated trajectories  
116 (Haller, 2002; Lekien and Ross, 2010; Rypina et al., 2021). This method uses 4 (in 2D) closest

117 neighbors to construct the Cauchy-Green tensor  $G = \begin{pmatrix} \Delta x_i \\ \Delta x_{o,j} \end{pmatrix}^T \begin{pmatrix} \Delta x_i \\ \Delta x_{o,j} \end{pmatrix}$ , whose largest eigenvalue  $\sigma$

118 is connected to

$$119 \quad \lambda = \frac{1}{T} \ln \sqrt{\sigma}. \quad (1)$$

120 Here  $\Delta x_{o,i}$  and  $\Delta x_i$  are the initial and final distance in the  $i^{\text{th}}$ -direction between neighboring  
121 trajectories. This algorithm requires dense regularly-spaced orthogonal grids of trajectories. For



122 the SPLASH dataset, we manually chose quadruplets of 4 neighboring trajectories that form a  
123 near-rectangle, define the local orthogonal coordinate system most strongly aligned with the axes  
124 of the near-rectangle, and then estimate FTLEs using eq. (1) for the center of mass of each  
125 quadruplet (Fig. 2 shows the quadruplets and their centers of mass locations).

126 A modification for unstructured meshes was described in Lekien and Ross (2010), where FTLE  
127 for each trajectory is estimated using its  $N$  closest neighbors as

$$128 \quad \lambda = \frac{1}{T} \ln \tilde{\sigma} \quad , \quad (2)$$

129 where  $\tilde{\sigma}$  is the largest positive singular value of a matrix

$$130 \quad \tilde{M} = DX_f (DX_0)^T (DX_0(DX_0)^T)^{-1}$$

131 which minimizes  $\|DX_f - M DX_0\|$ .

$$132 \quad \text{Here } DX_0 = \begin{pmatrix} x_1^0 - x_i^0 & \dots & x_N^0 - x_i^0 \\ y_1^0 - y_i^0 & \dots & y_N^0 - y_i^0 \\ z_1^0 - z_i^0 & \dots & z_N^0 - z_i^0 \end{pmatrix} \text{ and } DX_f = \begin{pmatrix} x_1^f - x_i^f & \dots & x_N^f - x_i^f \\ y_1^f - y_i^f & \dots & y_N^f - y_i^f \\ z_1^f - z_i^f & \dots & z_N^f - z_i^f \end{pmatrix} \text{ are matrices of the}$$

133 initial and final displacements between the trajectory and its  $N$  neighbors. Because the largest  
134 singular value of  $\tilde{M}$  is equal to the square root of the largest eigenvalue of  $\tilde{G} = \tilde{M}^T \tilde{M}$ , eq. (2) is  
135 the unstructured-mesh counterpart of eq. (1). We use the Delaunay triangulation partition to  
136 define closest neighbors for each drifter (Fig. 2 shows the Delaunay partition for the SPLASH  
137 dataset). The FTLE is then estimated using eq. (2) at each drifter's initial position using its  
138 Delaunay closest neighbors. When used together, a combination of these two methods – the  
139 regular and the unstructured mesh methods – allows estimating FTLEs both at the locations of  
140 each drifter and between neighboring quadruplets.



141

142 **b) Trajectory path length**

143 Trajectory path length  $L = \int ds = \int_{t_0}^{t_0+T} |\vec{u}(x(t), t)| dt$ , where  $ds$  is the incremental length of  
144 the infinitesimal trajectory segments. For drifter data, summation can be used instead of  
145 integration.  $L$  has been proposed by Rypina et al. (2011) as one of the “Trajectory Complexity  
146 measures” and by Mancho et al. (2013) as the “Lagrangian Descriptor” for identifying LCSs.  
147 Curves of near-constant  $L$  values with a large  $\nabla L$  in the perpendicular direction to the curve are  
148 indicative of the stable manifolds of hyperbolic trajectories (because trajectories on the manifold  
149 approach the hyperbolic trajectory and trajectories slightly off the manifold are repelled from it).  
150 This method is less mathematically rigorous than FTLEs and is frame-dependence, but it is  
151 commonly used due to its simplicity.

152

153 **c) Trajectory correlation dimension**

154 Trajectory correlation dimension ( $C$ ) is a measure of space occupied by a trajectory. In 2D, it  
155 varies from 0 for a point, to 1 for a curve, to 2 for a trajectory that densely fills an area.  $C$  can be  
156 estimated using a box counting algorithm, where the entire trajectory data set is first mapped  
157 onto a unit square, and the unit square is then repeatedly split into  $2^{-2m}$ ,  $m = 0, 1, \dots, M$  adjacent  
158 square boxes with side length  $s = 2^{-m}$  (we use  $M = 12$  in this paper). A distribution function is  
159 then computed for each trajectory as  $F_i(s) = \frac{1}{N_i^2} \sum (N_i^j(s))^2$  where  $N_i$  is the total number of  
160 points in the  $i^{\text{th}}$  trajectory and  $N_i^j$  is the number of points in the  $i^{\text{th}}$  trajectory that fall inside the  $j^{\text{th}}$   
161 box for a given  $s$ . The trajectory correlation dimension  $C_i$  for the  $i^{\text{th}}$  trajectory can then be  
162 estimated as the slope of  $F_i(s)$  vs.  $s$  in log-log coordinates. Just like trajectory path length,  $C$  is





163 another measure of “Trajectory Complexity” and has been proposed by Rypina et al. (2011) as a  
164 means for LCS identification. Similar to  $L$ , level curves of near-constant  $C$  with a large  $\nabla C$  in the  
165 perpendicular direction to the curve are indicative of the stable manifolds of hyperbolic  
166 trajectories.  $C$  is a more sensitive measure of “Trajectory Complexity” than  $L$  but is more  
167 computationally expensive. Just like  $L$ ,  $C$  is also frame dependent.

168

#### 169 **d) Trajectory encounter number and trajectory encounter volume**

170 Trajectory encounter volume  $V_{en}$  for a particular trajectory is a volume of fluid that gets in  
171 contact with a particular water parcel over a time interval  $T$  (Rypina and Pratt, 2017; Rypina et  
172 al., 2018). This is a frame-independent quantity. It quantifies the mixing potential of a flow and  
173 is related to the eddy or turbulent flow diffusivity  $\kappa$  (Rypina et al., 2018). The larger  $V_{en}$ , the  
174 more opportunities exist for a parcel to exchange properties with surrounding fluid. Smallest  $V_{en}$   
175 occur in isolated secluded regions of the flow such as eddy cores, and largest  $V_{en}$  occur in  
176 hyperbolic regions and along the stable manifolds of hyperbolic trajectories. Thus,  $V_{en}$  can be  
177 used to characterize both elliptic and hyperbolic LCSs.

178 For data sets containing a finite number of particle trajectories, encounter volume for a particular  
179 trajectory can be approximated by assigning small volumes  $\delta V_j$  to all trajectories and summing  
180 over those trajectories that come close to the particular trajectory:  $V_{en} \approx \sum \delta V_j$ . For regular grids  
181  $\delta V_j = \delta V = const$  and  $V_{en} = \delta V N_{en}$  where  $N_{en}$  is the encounter number – the number of  
182 trajectories that come close (i.e., within a small radius  $R$ ) to the particular trajectory. In our  
183 calculations, we use  $R = 1$  km and  $\delta V \approx 1$  km<sup>2</sup>, which is the square of the mean distance  
184 between the drifters’ release locations.

185



186 **e) Dilation**

187 Dilation is the velocity divergence averaged along a particle's trajectory,

188  $D = \frac{1}{T} \int_{t_0}^{t_0+T} \text{div}(u(x(t), t))$ . This frame-independent quantity was proposed by Huntley et al.

189 (2015) as a method for identifying clusters of material at the ocean surface. Trajectories with the

190 largest positive/negative  $D$  experience the strongest divergence/convergence and thus

191 repel/accumulate buoyant floating surface tracers (including drifters). For drifter data,

192 summation can be used instead of integration, and the Linear Least Squares method of Molinari

193 and Kirwan (1975) can be used to estimate  $\text{div}(u)$  at each point along each trajectory.

194

195 **f) Lagrangian-Averaged Vorticity Deviation (LAVD)**

196  $LAVD$  is the vorticity deviation with respect to the domain-averaged instantaneous vorticity,

197 averaged along a particle trajectory,  $LAVD = \frac{1}{T} \int_{t_0}^{t_0+T} |\omega(x(x_0, t) - \overline{\omega(t)})| dt$ . It was introduced

198 by Haller et al. (2016) as a frame-independent metric for identifying rotationally coherent

199 Lagrangian eddies, which correspond to a region contained within the outermost convex level

200 surface of  $LAVD$  surrounding a maximum. For drifter data, we again use summation instead of

201 integration and estimate vorticity using a Linear Least Squares method.

202

203 **g) Spectral Clustering**

204 The last method for identifying the LCSs that we will be testing using drifter data is the

205 optimized-parameter Spectral Clustering described in Filippi et al., 2021a;b (see also Shi and

206 Malik (2000), Hadjighasem et al. (2016) and references therein). This method aims at

207 identifying, within a given dataset of trajectories, clusters of trajectories that are most similar to



208 each other and, at the same time, most dissimilar from trajectories in other clusters. The method  
209 starts with the construction of a matrix of weights

210  $w_{ij} = \begin{cases} \frac{1}{r_{ij}} \\ w_{diag} \end{cases}$ , where  $r_{ij}$  is the time-average distance between  $i^{th}$  and  $j^{th}$  trajectory, and  $w_{diag}$  is

211 a large constant offset value (we use  $w_{diag} = \max(w_{ij}) \times 10^7$ ). Based on this matrix, the  
212 method used ideas from machine learning theory, specifically, N-cut matrix partitioning and K-  
213 means clustering algorithms, to identify the spectral clusters with the largest/smallest degree of  
214 intra-/inter-cluster similarity. Importantly, the optimized-parameter version of the Spectral  
215 Clustering method (Filippi et al., 2021a;b) that we are using automatically detects both the  
216 optimal number of clusters and the clusters sizes (based on the normalized eigengap between the  
217 eigenvalues of the generalized normalized Laplacian, as described in Filippi et al. (2021a)).  
218 Being based on the distances between trajectories, spectral clustering is frame-independent.

219

220 **h) Linear Least Squares (LLS) method for estimating drifter-based divergence and**  
221 **vorticity**

222 In order to estimate divergence and vorticity from drifters, we follow the approach of Rypina et  
223 al. (2021), where we first compute horizontal velocities from drifter positions using a centered  
224 finite-difference scheme and then apply the linear least squares (LLS) method of Molinari and  
225 Kirwan (1975) to estimate horizontal velocity gradients. LLS method is based on the Taylor  
226 expansion of velocity,  $U = DA$ , where  $U = [u_1, \dots, u_N]$  is a (known) vector containing the

227  $u$  – velocity at a given time  $t$  for each of the  $N$  drifters,  $D = \begin{pmatrix} 1 & x_1 - \bar{x} & y_1 - \bar{y} \\ \vdots & \vdots & \vdots \\ 1 & x_N - \bar{x} & y_N - \bar{y} \end{pmatrix}$  is a known

228 distance matrix containing instantaneous distances from each drifter to the center of mass of the



229 drifter distribution at time  $t$ , and  $A = \left[ \bar{u}, \frac{\partial u}{\partial x}, \frac{\partial u}{\partial y} \right]$  is the vector containing the unknown velocity  
230 derivatives at time  $t$  that can be estimated using the Moore-Penrose pseudo-inverse as  $A =$   
231  $(D^T D)^{-1} D^T U$  (and similarly for the v-component). The accuracy of the LLS method increases  
232 with increasing number of drifters and decreasing aspect ratio of the drifter configuration, i.e.,  
233 LLS works best for tight equidistant polygons with many drifters. Following Essink et al. (2021),  
234 we will refer to the LLS estimates as trustworthy (and mark them by colored circles) if there are  
235  $\geq 6$  drifters within a 3 –km radius, the center of mass of the drifter distribution is located within  
236 the polygon, and the polygon aspect ratio is  $\leq 6$ . If the aspect ratio condition is not satisfied (but  
237 the number of drifters, the distance, and the center of mass conditions are), we still compute LLS  
238 estimates but we refer to them as less trustworthy (and mark them by colored diamonds). In all  
239 other cases, we do not produce estimates of divergence and vorticity. Note that methods other  
240 than LLC can also be used to compute divergence and vorticity: divergence can be estimated as a  
241 rate of change of the area spanned by the drifter polygon, and both divergence and vorticity can  
242 be estimated using Green’s theorem as, respectively, the circulation around and total flux  
243 through the drifter polygon. Rypina et al. (2021) compared all three techniques in detail using  
244 both real and simulated drifters deployed at similar inter-drifter distances as the SPLASH drifters  
245 and observed good correspondence between all three techniques for clusters of 6 drifters as long  
246 as the drifters stayed within a few km of each other and the aspect ratio was reasonably small  
247 ( $\leq 5$ ). Because the LLC method was yielding slightly less noisy results for marginal inter-drifter  
248 distances and aspect ratios, here we show results for the LLS rather than other techniques.

249

### 250 3. Results



251 We start by qualitatively separating the motion of drifters into three stages. For about a day after  
252 deployment, all drifters started moving together in an anticyclonic fashion to the north and then  
253 northeast towards the coast (Fig. 1) – this is what we will refer to as the initial stage of motion.  
254 Upon approaching the shelf, the drifters halted their on-shore motion and split into two groups, a  
255 smaller northern group that headed northward along the coast and a larger southern group that  
256 moved southward. This splitting behavior was reminiscent of a hyperbolic motion in the vicinity  
257 of a hyperbolic trajectory, with a stable manifold emanating from a hyperbolic trajectory in the  
258 off-shore direction, and two unstable manifolds northward and southward from it in the along  
259 shore direction. As a result, a long and narrow filament roughly aligned with the coast is quickly  
260 formed just after 1 day. This filament contains about one third of all the drifters, with the rest of  
261 the drifters forming a less elongated and more compact blob just south-southwest of the filament.  
262 Some clustering of temporarily occurs at about 1 day near the southeastern corner of the drifter  
263 configuration but goes away later. The slow-down of the on-shore movement, the splitting into  
264 the north-south groups, and the formation of the elongated along-shore filament constitute the  
265 second stage of motion, which lasted from about 0.9 to about 1.25 days after the deployment.  
266 Finally, during the third stage of motion, the drifters started moving off-shore to the southwest.  
267 As they progress further from the coast, trajectories started exhibiting more looping and the  
268 drifters dispersed further apart from one another, although they still remained in an elongated  
269 filament configuration (not anymore aligned with the coast) all the way until day 5, which is the  
270 end time of this dataset.

271 Having split the drifter movement into 3 stages, we next apply our Lagrangian methods to  
272 trajectory segments from  $t_{start} = 0$  days until  $t_{end} = 0.5, 1,$  and 3 days, respectively (top,  
273 middle, and bottom row of panels in Figs. 3-9). The resulting fields highlight the dominant LCSs



274 that existed at the time of the drifter deployment (i.e., at  $t_{start} = 0$ ) and that governed the  
275 movement of drifters during the subsequent 0.5, 1, and 3 days, respectively. (A movie of the  
276 FTLEs at  $t_{start} = 0$  computed with progressively increasing  $t_{end}$  is included in the  
277 Supplementary Material.)

278 *FTLEs (Fig. 3):* During the initial stage of motion ( $t_{start} = 0$  days and  $t_{end} = 0.5$  days),  
279 FTLEs were generally smaller for drifters released in the north and south, and larger in between,  
280 especially in the west. As evident from the upper middle panel of Fig. 4 (FTLEs mapped to the  
281 current position of drifters on day 0.5), this behavior was dominated by the slightly larger  
282 separations (empty spaces) between drifters in the middle of the distribution and slightly tighter  
283 drifter distributions on the east and west sides. Later on, this small inhomogeneity in the early-  
284 time drifter separations became less important, and was overrun by other features. Specifically,  
285 during the intermediate stage ( $t_{start} = 0$  days and  $t_{end} = 1$  day), the largest FTLEs were  
286 observed along the northwestern edge of the release domain, containing drifters that split north-  
287 south upon approaching the coast and formed an elongated along-shelf filament. FTLEs were  
288 negative for drifters released near the middle of the northeastern edge of the release domain,  
289 which converged into a tight cluster in the southeastern corner of the drifter distribution at 1  
290 day. This feature was transient and disappeared as the drifters moved offshore. The rest of the  
291 release domain has small positive FTLE values; these were the drifters which did not experience  
292 strong along-shore alignment and formed a more compact group in the northern part of the  
293 drifter distribution at 1 day. Finally, during the third stage of motion ( $t_{start} = 0$  days and  
294  $t_{end} = 3$  days), as the drifters moved offshore and re-shaped into a northwest-southeast  
295 configuration, the only distinguishing feature of the FTLE field was the blue cluster near the  
296 central part of the release domain. This cluster contained trajectories that remained closer to each



297 other than other trajectories. When mapped to the current positions of the drifters at 3 days, these  
298 smallest blue FTLEs corresponded to a group of drifters in the western part of the distribution,  
299 i.e., a cluster of blue dots in the lower middle and right panels of Fig. 4. (Note that the northwest-  
300 southeast configuration at 3 days was mostly formed from the drifters located in the southern  
301 part of the distribution at 1 day, and so is different from the along-shelf “tail”.)

302 Overall, at all times the FTLE fields showed pronounced variations in values across the drifter  
303 distribution. Largest FTLEs indicated regions of strong drifter separation that, during the  
304 intermediate stage of motion, were reminiscent of stable manifolds of hyperbolic trajectories.  
305 Smallest FTLEs highlighted groups of drifters that stayed closer together compared to their  
306 neighbors. Transient negative FTLE regions were also present and highlighted groups of drifters  
307 temporarily converging into tight clusters (before spreading apart again later on). The FTLEs  
308 varied significantly with the increasing duration of trajectories, i.e., increasing  $t_{end}$ , suggesting  
309 that different flow features governed the movement of drifters during different stages of motion.  
310 The calculation of FTLEs was straightforward and computationally inexpensive, and by  
311 combining the structured and unstructured grid methods, we were able to obtain FTLE values at  
312 both drifter release positions and in between them, providing twice higher resolution compared  
313 to other methods.

314

315 *L* (Fig. 4): Trajectory path length *L* showed a monotonic increase in values with increasing  
316 latitude across the release domain at all times, with the largest/smallest values in the  
317 northwest/southeast. This large-scale gradient in *L* was dominated by the faster anticyclonic  
318 motion of the northwestern drifters at early times. This was reminiscent of a solid body rotation,  
319 where the northwestern drifters that were located further from the center of rotation than their



320 southeastern neighbors moved at a faster speed and thus covered a longer path length over a  
321 given time interval. (This effect could presumably be removed by recalculation of  $L$  in an  
322 appropriate rotating frame of reference, an operation that would not change the values of the  
323 FTLEs. Thus it is perhaps not surprising that the distributions of the two metrics differ in  
324 significant ways.) All other characteristic features, such as the splitting of trajectories into the  
325 northern and southern group at about 1 day, the formation of an elongated along-shelf filament,  
326 the transient convergence region, and the reshaping of the drifter configuration as it progressed  
327 further offshore had only minor effects on the resulting path length fields. We also looked at the  
328 gradient of the path length field as a means of identifying LCSs, but the gradient was noisy and  
329 did not yield any distinguished maxima. Thus, despite being easy to compute and straightforward  
330 to interpret, the path length  $L$  was only marginally useful in identifying the dominant LCSs.

331

332 *CD* (Fig. 5): Results for the trajectory correlation dimension  $CD$  were generally similar to those  
333 for the trajectory path length, in that  $CD$  was also dominated by the across domain gradient from  
334 northwest to southeast, and the distribution of  $CD$  did not change dramatically in time. Being a  
335 more sensitive measure of the trajectory complexity than  $L$ ,  $CD$  exhibited a slightly stronger  
336 variability across the domain. This sensitivity of  $CD$  came at a cost of being more  
337 computationally expensive than  $L$ , and, in the end, was still not enough to identify the LCSs  
338 responsible for neither the formation of the elongated filament at 1 day, nor the transient  
339 convergence zones just after 1 day, nor the suppressed separation between trajectories coming  
340 from the central part of the domain at 3 days. Overall,  $CD$  was no more useful than  $L$  in  
341 identifying the LCS, and, like  $L$ , had the same frame dependence issues.

342





343  $V_{en}$  (Fig. 6): The encounter volume  $V_{en}$  showed a lot of variability across the domain and was  
344 able to successfully highlight several different flow features governing the movement of drifters  
345 at different stages of motion. During the initial stage,  $V_{en}$  had largest values in the southern part  
346 of the release domain. From the top middle panel (the map of  $V_{en}$  at the current position of the  
347 drifters) we observed that these enhanced values were caused by the tighter clustering of drifters  
348 (so that they were able to meet more neighbors). During the intermediate stage of motion, the  
349 distribution of  $V_{en}$  changed, and the largest values migrated to the northeastern edge of the  
350 release domain. This was associated with the transient convergence zone (that we also observed  
351 in the FTLE fields); trajectories released in that area converged into a tight cluster located at the  
352 southeastern corner of the drifter distribution at 1 day (2<sup>nd</sup> row, middle panel). The elongated  
353 along-shore filament seen at 1 day contained smallest  $V_{en}$  values since trajectories in the  
354 filament did not encounter many neighbors. Trajectories that headed north after approaching the  
355 coast at 1 day never caught up with the rest of the distribution, always staying behind, i.e., to the  
356 north from the rest of the drifters. Thus, these drifters experienced the least amount of encounters  
357 and, during the third stage of motion, had the smallest  $V_{en}$  values. Apart from this low-  
358 encounter-number group, there were no other pronounced features in the  $V_{en}$  field during the  
359 third stage of motion.

360 It is interesting to compare and contrast  $V_{en}$  with FTLEs, which became sort of a benchmark for  
361 the LCS detection problems, being frame independent, commonly used, and easy to compute.  
362 There are significant differences between the distributions of the two metrics, reflecting  
363 differences in what the two are actually measuring. While both FTLEs and  $V_{en}$  are sensitive to  
364 flow convergence/divergence, trajectory clustering, and hyperbolic behavior, one of the key  
365 differences between them is that  $V_{en}$  is a time-integrated measure that depends on the behavior of



366 trajectories over the entire time interval between the initial and final times, whereas FTLEs only  
367 depend on the initial and final positions of drifters (i.e., FTLEs do not care how trajectories got  
368 to their final positions, whereas  $V_{en}$  does). For example, even though trajectories comprising the  
369 low-FTLE blue cluster in the western part of the distribution at 3 days have come close together  
370 at that time, over a time frame of 3 days they experienced no more trajectory encounters than  
371 many other trajectories outside of that blue FTLE cluster (and thus were not standing out in the  
372  $V_{en}$  field).

373 Overall, the encounter volume  $V_{en}$  proved to be an interesting frame-independent diagnostic that  
374 was sensitive to both enhanced clustering, hyperbolic behavior, and flow convergence, and was  
375 complementary to FTLEs.

376

377 *D* (Fig. 7): The challenge with computing dilation  $D$  (as well as  $LAVD$ ) for real drifters is the  
378 inability to reliably estimate divergence (vorticity) for isolated drifters and drifters forming  
379 strongly elongated polygons. This was not a problem for SPLASH drifters during the early stage  
380 of motion but became an issue as the drifters started to spread apart and formed elongated  
381 filaments. During the initial stage of motion (top row), the most pronounced feature of the  $D$   
382 field was the negative cluster in the southern corner of the release domain, which contained  
383 drifters that converged more than their neighbors. A similar feature has been identified by  $V_{en}$  as  
384 the high-encounter-volume region. The rest of the domain had near-zero dilation. During the  
385 second stage of motion (middle row), the negative dilation in the south diminished, and another  
386 convergent negative- $D$  region appeared along the northeastern edge and eastern corner of the  
387 release domain. This is reminiscent of the negative-FTLE / high- $V_{en}$  region in the middle rows of  
388 Figs. 3 and 6. Trajectories released there converged into the southeastern corner of the drifter



389 distribution at 1 day. Around this time, an increasing number of trajectories started having  
390 unreliable divergence values; for example, divergence and thus dilation, could not anymore be  
391 reliably computed for the northern group of trajectories, which became too few and too sparse.  
392 During the third stage of motion, this problem became even more important and by day 3, the  
393 dilation field was undefined for about half of the trajectories. The resulting  $D$  field was noisy and  
394 did not exhibit any pronounced features.

395 Overall, dilation  $D$  was useful in highlighting the convergence zones during the first two stages  
396 of motion, but numerical difficulties associated with reliably estimating divergence for sparse  
397 datasets and elongated drifter configurations made it challenging to compute  $D$  over long time  
398 intervals from real drifters.

399

400 *LAVD* (Fig. 8): During the first stage of motion, the strongest feature in the *LAVD* map was the  
401 red large-*LAVD* region near the southern corner of the release domain. This area coincided  
402 roughly with the negative- $D$  and large- $V_{en}$  in Figs. 6-7. During the second stage of motion, this  
403 feature diminished in intensity and a second high-*LAVD* region appeared near the eastern corner  
404 of the domain. Again, a similar region has been highlighted by low FTLEs, high  $V_{en}$ , and  
405 negative  $D$ , although *LAVD* emphasized the eastern corner rather than the entire northeastern  
406 edge of the release domain. Trajectories starting there converged into a tight cluster near the  
407 southeastern corner of the drifter distribution at 1 day. It is interesting that *LAVD* identified  
408 similar regions as FTLEs,  $V_{en}$ , and  $D$ , despite the fact that clustering behavior and flow  
409 convergence do not necessarily need to be associated with increased vorticity deviation. In our  
410 case, clustering and convergence did coincide with increased vorticity deviation, suggesting that  
411 perhaps a small-scale eddy or recirculation that was affecting this particular cluster of drifters



412 might have been responsible for all of these effects. (Note that interpreting the vorticity deviation  
413 as vorticity is only possible when the domain-averaged background vorticity,  $\bar{\omega}$ , is small, which  
414 was not always the case for the SPLASH drifters.) Finally, during the third stage of motion  
415 (bottom row), the map of *LAVD* became gappy (because, similar to the challenges with dilation,  
416 here we could not reliably estimate *LAVD* for about half of the drifters) and showed no  
417 distinguished regions. However, when mapped to the current position of the drifters (lower  
418 middle panel), the cluster in the middle of the drifter distribution showed larger *LAVD* values  
419 than clusters to the northwest and southeast (but since trajectories forming the middle cluster  
420 came from different parts of the release domain, this feature did not stand out in the left panel).

421 Overall, during the first two stages of motion, *LAVD* highlighted two regions with enhanced  
422 *LAVD* values. While large *LAVD* does not generally indicate convergence, in our case both  
423 regions were strongly convergent. At later times, vorticity estimation became less reliable, and it  
424 became harder to distinguish coherent features in the sparse and noisy map of *LAVD*. Note that  
425 our high-*LAVD* regions differed from the classical examples of coherent rotational eddies. Our  
426 regions were not circular, did not have a single maximum, and were too noisy to identify the  
427 outermost convex contour level (which marks the outer edge of the coherent rotational eddies in  
428 the standard application of the *LAVD* technique). Thus we cannot call these high-*LAVD* features  
429 Lagrangian coherent eddies.

430

431 *Spectral Clustering (Fig 9)*: At early times, the number of coherent clusters identified by the SC  
432 algorithm was quite large (12), although some clusters only contained a few drifters. (Recall that  
433 the optimized-parameter SC is able to autonomously identify the optimal number and optimal  
434 size of the clusters, without input from the user). Among the detected clusters, the yellow cluster



435 located in the south-southwest of the release domain is perhaps the most noteworthy because it  
436 resembled the low-FTLE / large- $V_{en}$ / negative- $D$ / large- $LAVD$  region that contained trajectories  
437 that stayed close together during the initial stage of motion. As the drifters entered the second  
438 stage of motion, the number of identified coherent clusters decreased to 6. Most of the release  
439 domain was split between two large clusters – the cyan cluster in the north-northeast containing  
440 drifters attracted by the convergence region (i.e., drifters that converged/came close to the  
441 southeastern corner of the drifter distribution at 1 day), and the green cluster in the south of the  
442 release domain containing drifters that did not feel the pull of that convergence zone. The  
443 remainder of the domain, i.e., the northwestern edge of the domain that mostly contained the  
444 trajectories forming an elongated along-shore filament, was split into 4 more clusters. Finally, at  
445 the third stage of motion, the drifters were split into 8 clusters, and the grouping was most  
446 straightforward to interpret by looking at the lower middle panel. All trajectories in the western  
447 cluster were blue (these trajectories came from the central and southern portion of the domain in  
448 the bottom left panel), with the yellow cluster to the southeast of it (these trajectories came from  
449 around the periphery of the blue cluster in the bottom left panel), and with the orange group  
450 further to the southeast of the yellow cluster (most orange trajectories originate from the  
451 northeastern edge of the release domain in the bottom left panel). The remaining 5 clusters only  
452 contained 1 or 2 trajectories.

453 Overall, the spectral clustering algorithm seems to have identified physically-meaningful and  
454 intuitively-clear coherent clusters; the movement was similar for drifters within each cluster and  
455 dissimilar between the clusters. There were also good correspondences between the spectral  
456 clusters and coherent featured highlighted by other methods.

457



458 **4. Summary and Discussion**

459 SPLASH drifter experiment provided the long-awaited opportunity to test the performance of  
460 different dynamical systems techniques with real, rather than simulated, ocean drifters. Although  
461 many other drifter data sets are available for various regions of the World Ocean, drifters are  
462 typically released by a handful here and there, and the resulting data is typically inadequate for  
463 mapping out the LCS. For example, the NOAA's Global Drifter Program data set contains  
464 several thousands of near-surface drifter trajectories released between 1971 and today, but the  
465 density of the drifter distribution at any given time is only about 1 per 5-by-5 deg box, which is  
466 too sparse to identify even mesoscale LCSs.

467 Three qualitatively-different stages of motion were evident in the SPLASH drifter data. During  
468 the first stage, all drifters moved anticyclonically toward the coast. During the second stage, the  
469 drifters halted their on-shore motion, split north-south, and formed an elongated along-shelf  
470 filament. During the third stage, the drifters moved off-shore, rearranging themselves into a  
471 northwest-southeast configuration. As the character of drifter movement changed with time, the  
472 maps of the Lagrangian metrics and the resulting LCSs that they highlighted changed as well. In  
473 order to capture this time-dependence, we have applied the Lagrangian metrics to segments of  
474 trajectories from fixed  $t_{start} = 0$  days to variable  $t_{end} = 0.5, 1, \text{ and } 3$  days, respectively.  
475 When the Lagrangian metrics were mapped back to the initial positions of drifters at  $t_{start}$ , the  
476 resulting maps highlighted the dominant LCS which existed at the time of the deployment within  
477 the deployment domain, and which govern the subsequent motion of drifters over the  
478 corresponding time interval. The fact that the results for any particular measure differed between  
479 the three time intervals is consistent with submesoscale dynamics, where fronts, small eddies,  
480 and filaments form, evolve, and disappear on time scales of days or less.



481 The Lagrangian techniques we have examined include FTLEs, trajectory path length, trajectory  
482 correlation dimension, trajectory encounter number, dilation,  $LAVD$ , and optimized-parameter  
483 spectral clustering. This list was motivated by Hadjighasem et al. (2017) and is by no means  
484 exhaustive, but it includes a variety of commonly-used methods that are based on different  
485 properties of trajectories, make use of the different definitions of coherence, and thus aim to  
486 identify different types of LCSs. Interestingly, despite the differences in their underlying  
487 principles and methodologies, many of these methods identified similar features within the  
488 SPLASH drifter data set.

489 Among the most prominent features that were highlighted by multiple methods were: 1) the  
490 region near the northwestern edge of the release domain (red FTLEs, blue  $V_{en}$ , a group of  
491 spectral clusters other than dark blue), which contained trajectories that split north-south upon  
492 approaching the shelf and formed an elongated along-shelf filament at about 1 day; 2) the very  
493 strong but transient convergence region located near the northeastern edge of the release domain  
494 (negative FTLEs, large  $V_{en}$ , strongly negative dilation, cyan spectral cluster), which contained  
495 trajectories that converged into a tight cluster at about 1 day; and 3) the region in the  
496 central/southern part of the release domain (small FTLEs, blue spectral cluster), which contained  
497 trajectories that remained close to each other starting from 2.5 days and onward.

498 Although all of the identified structures were noisier and more complex than the classical elliptic  
499 and hyperbolic LCSs in textbook examples, some of the features bore resemblance to their  
500 classical counterparts. For example, the north-south splitting of trajectories starting within the  
501 red FTLE region near the northwestern edge of the domain was qualitatively similar to the  
502 behavior of trajectories near a hyperbolic region, where particles approach the hyperbolic  
503 trajectory along a stable manifold and then split and move away from the hyperbolic trajectory



504 along the two unstable directions. The detected large-FTLE region near the northwestern edge of  
505 the release domain might thus possibly indicate the presence of a stable manifold in this region.

506 From the standpoint of numerical efficiency, FTLEs and  $L$  were the least computationally  
507 expensive, whereas  $CD$ ,  $V_{en}$ , and Spectral Clustering were the most computationally expensive.  
508 However, with only 135 trajectories, the differences in the amount of time required to apply each  
509 technique were not critical. More importantly, FTLEs had the advantage of providing values at  
510 the positions of each drifter as well as between the neighboring drifters, effectively yielding  
511 output fields with twice the resolution of the other methods. FTLEs were also less affected by the  
512 gaps in GPS transmissions along trajectories, because the estimation of FTLEs at a particular  
513 time only required knowing the initial and the current positions of the drifters, rather than  
514 requiring the information about the entire trajectory up to that time, as in the case of all other  
515 methods - path length, correlation dimension, encounter number, dilation,  $LAVD$ , and spectral  
516 clusters.

517 It is interesting to note that the two frame-dependent methods –  $L$  and  $CD$ , which were  
518 dominated by the large-scale gradient across the entire release domain and did not highlight any  
519 submesoscale features – were the least useful in identifying LCSs.

520 Massive drifter releases such as SPLASH are extremely useful for improving our understanding  
521 of the transport and exchange processes at submesoscale. Specifically, data from the SPLASH  
522 and other similar experiments have been used for estimating diffusivity and studying particle  
523 spreading regimes at submesoscale (Poje et al., 2014; Beron-Vera and LaCasce, 2016). We have  
524 shown that a simultaneous release of about 100 drifters provides a glimpse of the dominant  
525 Lagrangian Coherent Structures that govern the transport of water and the movement of drifters.





526 SPLASH experiment was not specifically focused on identifying LCSs, so the drifter release  
527 locations and timings were not optimized for capturing the underlying LCSs. Our analysis  
528 suggested that, luckily, a stable manifold of a hyperbolic trajectory was likely present in the  
529 northwestern edge of the domain spanned by the drifters at the time of their release and persisted  
530 for at least the first 1-1.5 days of the experiment. As explained above, this feature manifested  
531 itself as a high-FTLE region and was characterized by the north-south splitting of trajectories  
532 around day 1. However, no clear elliptic LCSs (i.e., coherent eddy cores) were identified by any  
533 of the methods, even though an anticyclone was likely present in the region (based on the  
534 numerical model simulations and the clockwise movement of drifters during the first day after  
535 release). It is difficult to say whether this anticyclone did not possess a Lagrangian core, or the  
536 core was located outside of the drifter release domain, or whether the core was not properly  
537 resolved by the SPLASH drifters. In the future, it would be interesting to repeat the experiment  
538 with the drifter deployment site and the release pattern optimized for capturing specific LCSs  
539 whose presence could have been predicted based on a model or satellite data.

540 The very rapid nature of evolution at submesoscales may cause an evenly spaced array of drifters  
541 to rapidly collect into filaments, making it difficult to continue to accurately compute certain  
542 Lagrangian measures. In SPLASH experiment, for example, the nearly-rectangular deployment  
543 mesh of drifters (which took quite a bit of effort to achieve) eroded into an elongated filament  
544 over a time scale of about a day. Note, however, that it is precisely this rapid filamentation  
545 process and the rapid deformation of the initial mesh that gives rise to the strong, pronounced,  
546 and detectable LCSs.

547 Finally, in order to investigate the robustness and reliability of the real-drifter-derived LCS, we  
548 have simulated the SPLASH drifter dataset in a model and then compared the resulting



549 SPLASH-like drifter-based LCS to those computed using dense regular orthogonal grids of  
550 trajectories (we refer to the latter as true model fields). We used the operational data-assimilative  
551 Navy Coastal Ocean Model (NCOM) forecasting model for this purposes  
552 (<https://data.gulfresearchinitiative.org/data/R4.x265.245:0002>). Comparison between SPLASH-  
553 like and true model fields showed good agreement, the Lagrangian metrics for the real and  
554 simulated SPLASH drifter were of the same magnitude, and the overall geometries and types of  
555 the coherent features were similar in the model and in the real ocean, suggesting that SPLASH-  
556 based fields were robust and reliable. Detailed comparisons can be found in Supplementary  
557 Material.

558 **Acknowledgements:** Many thanks to Gregg Jacobs of NRL Stennis and William Nichols at  
559 GRIIDC for sharing the output of the NCOM model. We are grateful to Margaux Filippi and  
560 Alireza Hadjigjaseem for their help with the spectral clustering code. IR and LP would like to  
561 acknowledge support from the ONR CALYPSO grant #N000141812417. TG is thankful to ONR  
562 for supporting his NAVY Master's program fellowship at WHOI. TO was supported by ONR  
563 CALYPSO grant #N000141812138.

#### 564 **Data Availability Statement**

565 Data from the Submesoscale Processes and Lagrangian Analysis on the Shelf (SPLASH) surface  
566 drifters used in this paper is available from:

567 <https://data.gulfresearchinitiative.org/data/R4.x265.000:0074>.

568 The NCOM model output fields used in this paper are available from:

569 <https://data.gulfresearchinitiative.org/data/R4.x265.245:0002>.



570 **Author Contribution Statement:** IR led the overall effort and primarily wrote the manuscript,

571 TG performed estimation of most Lagrangian metrics, LP and TO contributed to the

572 interpretation of the results and editing of the manuscript.

573 **Competing interests Statement:** no competing interests

574

575

576

577

578

579

580

581

582

583

584

585



586 **References:**

587

588 Balasuriya, S., Ouellette, N.T. and Rypina, I.I.: Generalized Lagrangian coherent  
589 structures. *Physica D: Nonlinear Phenomena*, 372, pp.31-51, 2018.

590

591 Beron-Vera, F.J. and LaCasce, J.H.: Statistics of simulated and observed pair separations in the  
592 Gulf of Mexico. *Journal of Physical Oceanography*, 46(7), pp.2183-2199, 2016.

593

594 Filippi, M., Rypina, I.I., Hadjighasem, A. and Peacock, T.: An Optimized-Parameter Spectral  
595 Clustering Approach to Coherent Structure Detection in Geophysical Flows. *Fluids*, 6(1), p.39,  
596 2021.

597

598 Filippi, M., Hadjighasem, A., Rayson, M., Rypina, I.I., Ivey, G., Lowe, R., Gilmour, J. and  
599 Peacock, T.: Investigating transport in a tidally driven coral atoll flow using Lagrangian coherent  
600 structures. *Limnology and Oceanography*, 66(11), pp.4017-4027, 2021.

601

602 Froyland, G. and Padberg-Gehle, K.: A rough-and-ready cluster-based approach for extracting  
603 finite-time coherent sets from sparse and incomplete trajectory data. *Chaos: An Interdisciplinary  
604 Journal of Nonlinear Science*, 25(8), p.087406, 2015.

605

606 Jacobs, G.A., Bartels, B.P., Bogucki, D.J., Beron-Vera, F.J., Chen, S.S., Coelho, E.F., Curcic,  
607 M., Griffa, A., Gough, M., Haus, B.K. and Haza, A.C.: Data assimilation considerations for



608 improved ocean predictability during the Gulf of Mexico Grand Lagrangian Deployment  
609 (GLAD). *Ocean Modelling*, 83, pp.98-117, 2014.

610

611 Hadjighasem, A., Karrasch, D., Teramoto, H. and Haller, G.: Spectral-clustering approach to  
612 Lagrangian vortex detection. *Physical Review E*, 93(6), p.063107, 2016.

613

614 Hadjighasem, A., Farazmand, M., Blazeovski, D., Froyland, G. and Haller, G.: A critical  
615 comparison of Lagrangian methods for coherent structure detection. *Chaos: An Interdisciplinary  
616 Journal of Nonlinear Science*, 27(5), p.053104, 2017.

617

618 Haller, G.: Lagrangian coherent structures from approximate velocity data. *Physics of  
619 fluids*, 14(6), pp.1851-1861, 2002.

620

621 Haller, G.: An objective definition of a vortex. *Journal of fluid mechanics*, 525, pp.1-26, 2005.

622

623 Haller, G.: Lagrangian coherent structures. *Annual Review of Fluid Mechanics*, 47, pp.137-162,  
624 2015.

625

626 Haller, G. and Yuan, G.: Lagrangian coherent structures and mixing in two-dimensional  
627 turbulence. *Physica D: Nonlinear Phenomena*, 147(3-4), pp.352-370, 2000.

628

629 Haller, G., Hadjighasem, A., Farazmand, M. and Huhn, F.: Defining coherent vortices  
630 objectively from the vorticity. *Journal of Fluid Mechanics*, 795, pp.136-173, 2016.



631

632 Huntley, H.S., Lipphardt Jr, B.L., Jacobs, G. and Kirwan Jr, A.D.: Clusters, deformation, and  
633 dilation: Diagnostics for material accumulation regions. *Journal of Geophysical Research:*  
634 *Oceans*, 120(10), pp.6622-6636, 2015.

635

636 Lekien, F. and Ross, S.D.: The computation of finite-time Lyapunov exponents on unstructured  
637 meshes and for non-Euclidean manifolds. *Chaos: An Interdisciplinary Journal of Nonlinear*  
638 *Science*, 20(1), p.017505, ., 2010.

639

640 Laxague, N., Özgökmen, T. M., Haus, B. K., Novelli, G., Shcherbina, A., Sutherland, P.,  
641 Guigand, C., Lund, B., Mehta, S., Alday, M., Molemaker, J.: Observations of near-surface  
642 current shear help describe oceanic oil and plastic transport. *Geophysical Research Letters*,  
643 45(1), 245-249, 2018.

644

645 Lund, B., Haus, B.K., Graber, H.C., Horstmann, J., Carrasco, R., Novelli, G., Guigand, C.,  
646 Mehta, S., Laxague, N., and Özgökmen, T.M.: Marine X-Band Radar Currents and Bathymetry:  
647 An Argument for a Wave Number-Dependent Retrieval Method. *JGR-Oceans*, 125(2),  
648 [e2019JC015618](https://doi.org/10.1029/2019JC015618), 2020.

649

650 Mancho, A.M., Wiggins, S., Curbelo, J. and Mendoza, C.: Lagrangian descriptors: A method for  
651 revealing phase space structures of general time dependent dynamical systems. *Communications*  
652 *in Nonlinear Science and Numerical Simulation*, 18(12), pp.3530-3557, 2013.



653 Martin, P.J.: *Description of the navy coastal ocean model version 1.0*. Naval Research Lab  
654 Stennis Space Center MS, 2000.  
655  
656 Molinari, R. and Kirwan Jr, A.D.: Calculations of differential kinematic properties from  
657 Lagrangian observations in the western Caribbean Sea. *Journal of Physical Oceanography*, 5(3),  
658 pp.483-491, 1975.  
659  
660 Özgökmen, T.M., Bracco, A., Chassignet, E.P., Chang, H., Chen, S.C., D'Asaro, E., Fox-  
661 Kemper, B., Haza, A.C., Jacobs, G., Novelli, G. and Poje, A.: Basin-Scale and Near-Surface  
662 Circulation in the Gulf of Mexico. In *International Oil Spill Conference* (Vol. 2021, No. 1, p.  
663 686903), 2021.  
664  
665 Poje, A.C., Özgökmen, T.M., Lipphardt, B.L., Haus, B.K., Ryan, E.H., Haza, A.C., Jacobs, G.A.,  
666 Reniers, A.J.H.M., Olascoaga, M.J., Novelli, G. and Griffa, A.: Submesoscale dispersion in the  
667 vicinity of the Deepwater Horizon spill. *Proceedings of the National Academy of*  
668 *Sciences*, 111(35), pp.12693-12698, 2014.  
669  
670 Rypina, I.I., Pratt, L.J., Pullen, J., Levin, J. and Gordon, A.L.: Chaotic advection in an  
671 archipelago. *Journal of Physical Oceanography*, 40(9), pp.1988-2006, 2010.  
672  
673 Rypina, I.I., Scott, S.E., Pratt, L.J. and Brown, M.G.: Investigating the connection between  
674 complexity of isolated trajectories and Lagrangian coherent structures. *Nonlinear Processes in*  
675 *Geophysics*, 18(6), pp.977-987, 2011.



676

677 Rypina, I.I. and Pratt, L.J.: Trajectory encounter volume as a diagnostic of mixing potential in  
678 fluid flows. *Nonlinear Processes in Geophysics*, 24(2), pp.189-202, 2017.

679

680 Rypina, I.I., Llewellyn Smith, S.G. and Pratt, L.J.: Connection between encounter volume and  
681 diffusivity in geophysical flows. *Nonlinear Processes in Geophysics*, 25(2), pp.267-278, 2018.

682

683 Rypina, I.I., Getscher, T.R., Pratt, L.J. and Moure, B.: Observing and quantifying ocean flow  
684 properties using drifters with drogues at different depths. *Journal of Physical*

685 *Oceanography*, 51(8), pp.2463-2482, 2021.

686

687 Samelson, R.M. and Wiggins, S.: *Lagrangian transport in geophysical jets and waves: The*  
688 *dynamical systems approach* (Vol. 31). Springer Science & Business Media, 2006.

689

690 Shadden, S.C., Lekien, F. and Marsden, J.E.: Definition and properties of Lagrangian coherent  
691 structures from finite-time Lyapunov exponents in two-dimensional aperiodic flows. *Physica D:*

692 *Nonlinear Phenomena*, 212(3-4), pp.271-304, 2005..

693

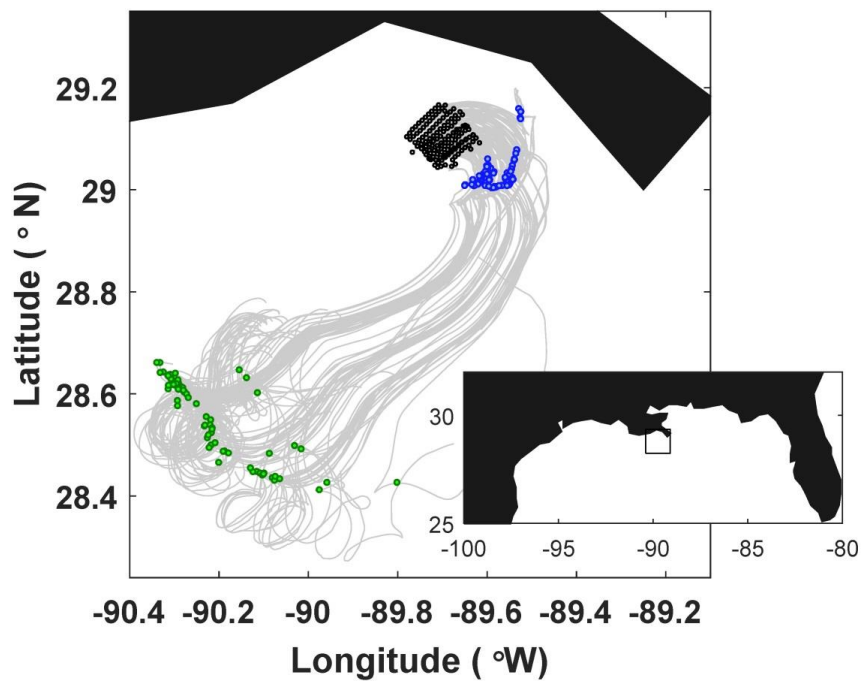
694 Shi, J. and Malik, J.: Normalized cuts and image segmentation. *IEEE Transactions on pattern*  
695 *analysis and machine intelligence*, 22(8), pp.888-905, 2000.

696





697 Solodoch, A., Molemaker, J. M., Srinivasan, K., Berta, M., Marie, L., Jagannathan, A.:  
698 Observations of Shoaling Density Current Regime Changes in Internal Wave Interactions. J.  
699 Phys. Oceanogr., 50(6), 1733-1751, 2020.  
700  
701 Von Luxburg, U.: A tutorial on spectral clustering. *Statistics and computing*, 17(4), pp.395-416,  
702 2007..  
703  
704  
705  
706  
707



708

709 **Figure 1.** Trajectories of the SPLASH drifters, with their positions at the release time, 1 day, and 3 days shown by black, blue,

710 and green dots, respectively. The inset shows the geographical location of the experiment cite, with black box indicating the

711 domain shown in the main panel.

712

713

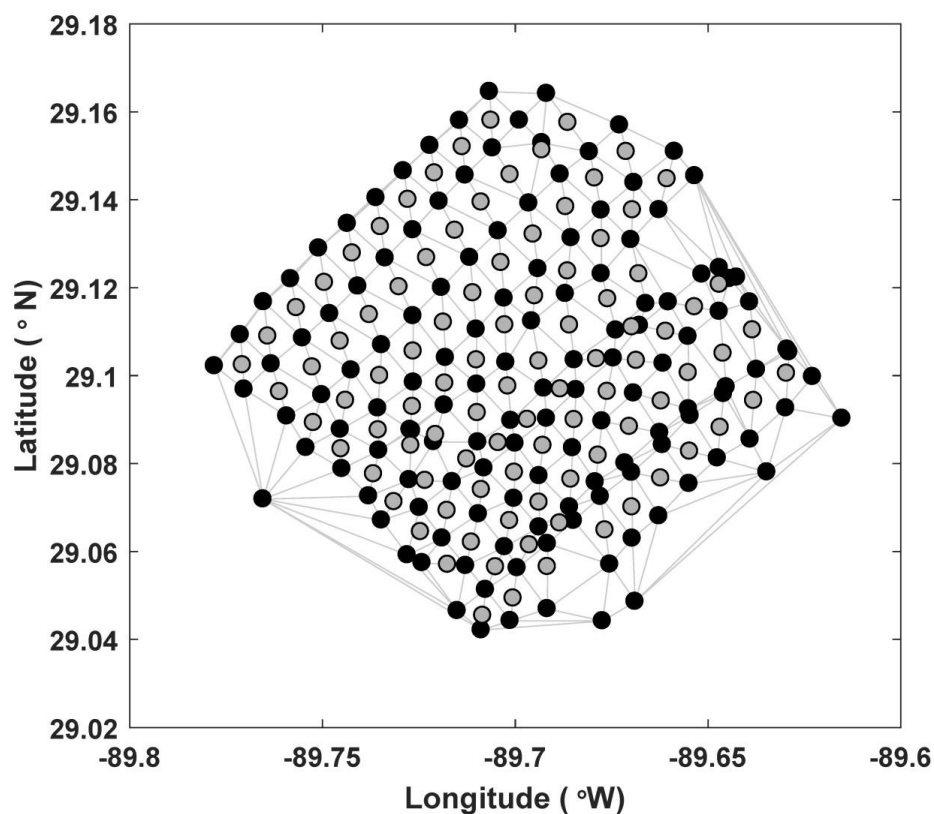
714

715

716

717

718



719

720 Figure 2. Release locations of the SPLASH drifters (black dots) with the Delaunay delineation (grey lines) used to define the  
721 closest neighbors for estimating FTLEs at the drifter positions using the unstructured grid method. Grey circles show  
722 locations between the drifters, at which FTLEs were estimated via the structured grid method (using a quadruplet of black  
723 drifters around each grey dot).

724

725

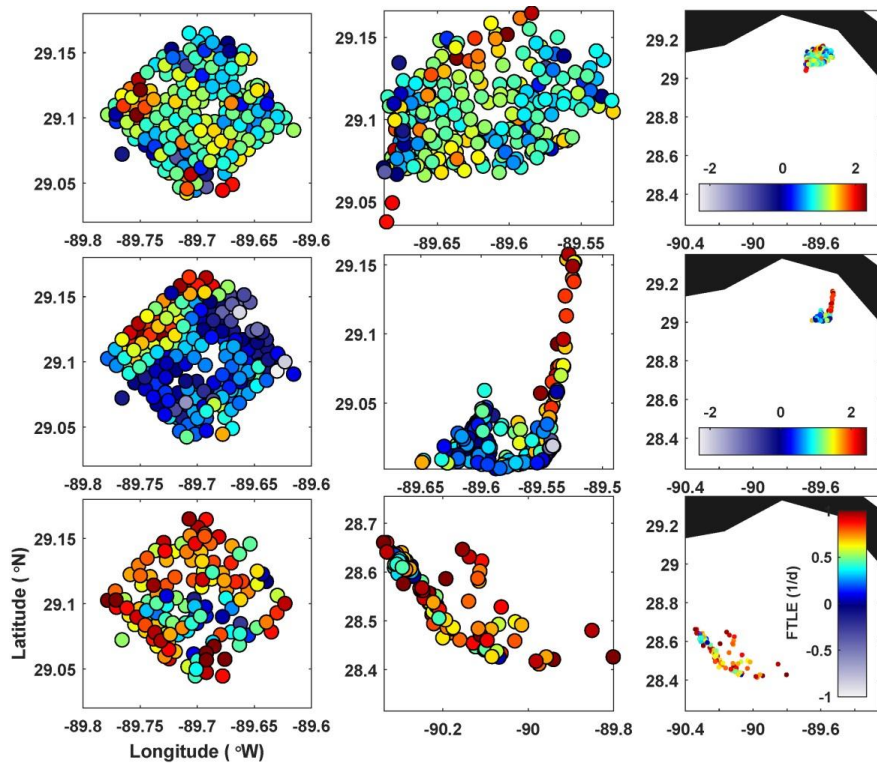
726

727

728



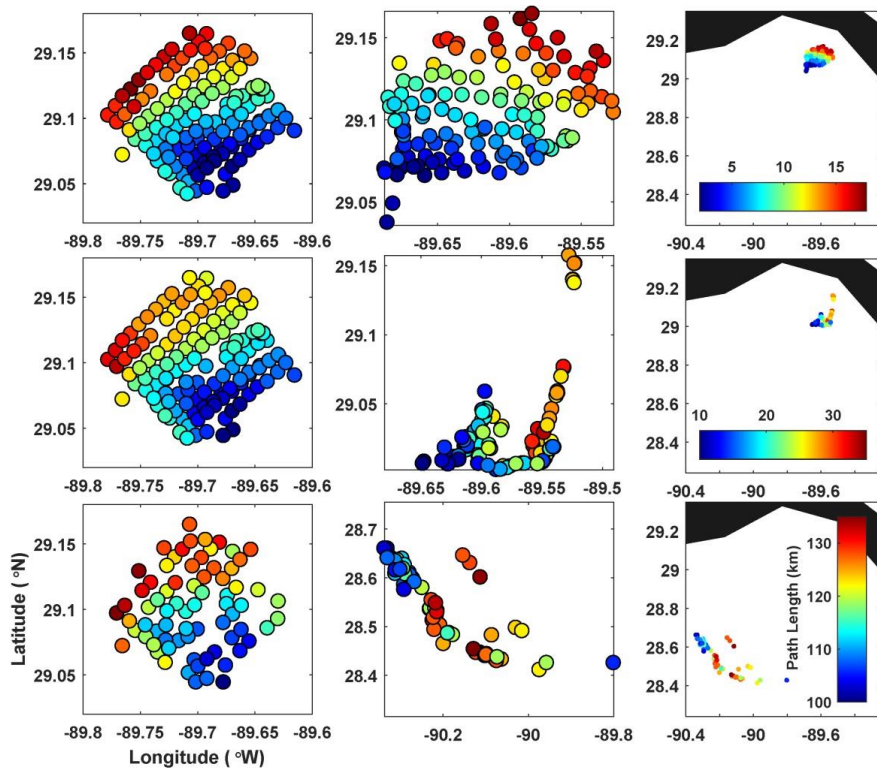
729



730

731 **Figure 3. Real-drifter-based FTLEs at (top) 0.5, (middle) 1, and (bottom) 2 days, mapped to the initial (left) and current**

732 **(middle and right) positions of the drifters.**

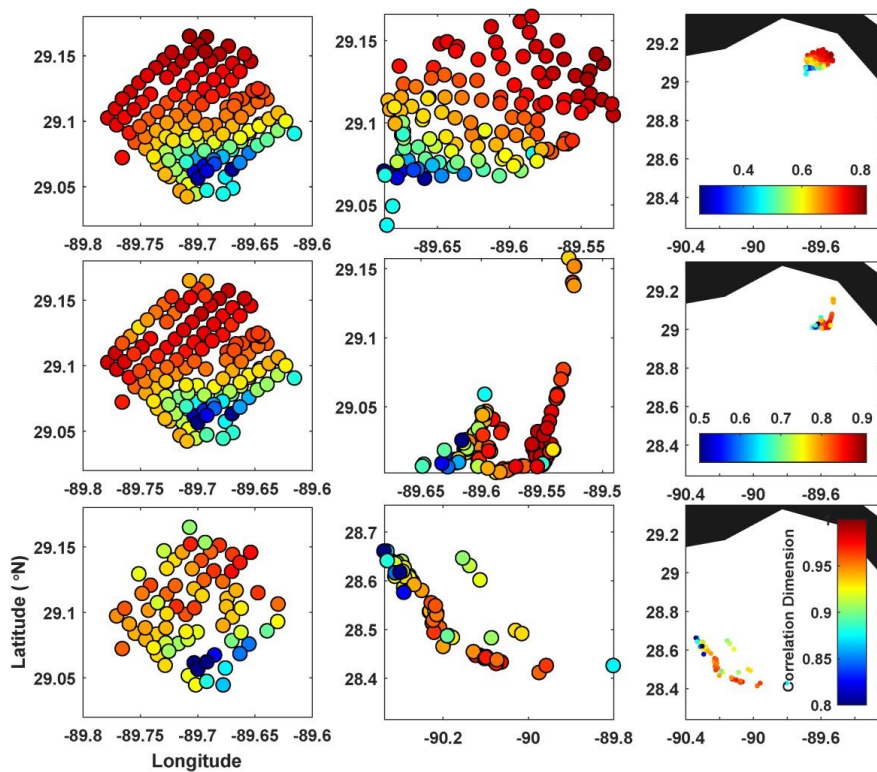


733

734 **Figure 4. Real-drifter-based path length at (top) 0.5, (middle) 1, and (bottom) 3 days, mapped to the initial (left) and current**

735 **(middle and right) positions of drifters.**

736

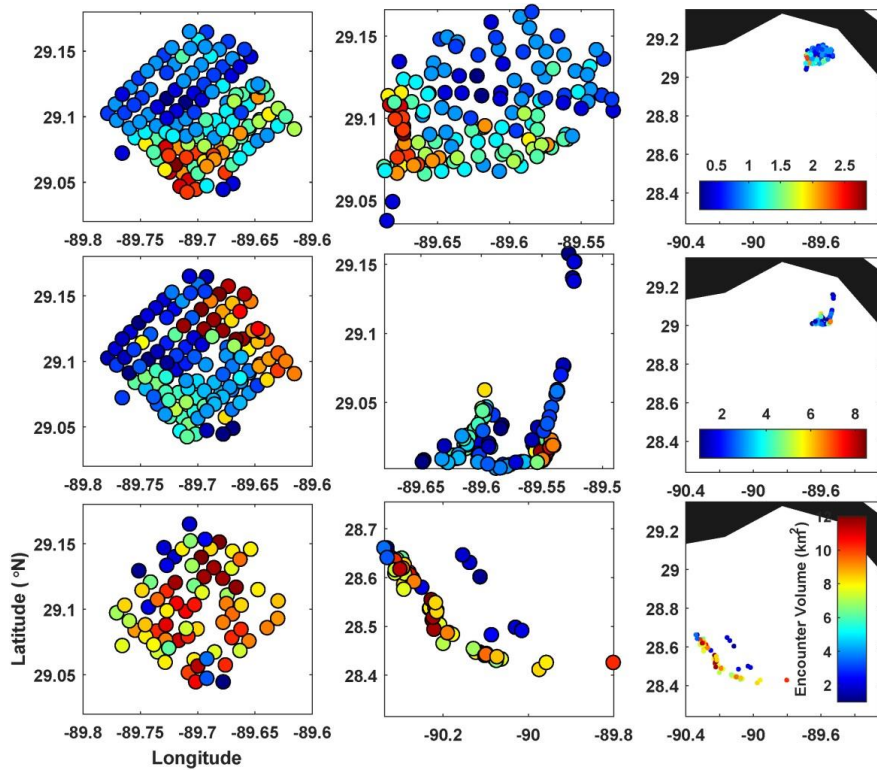


737

738 **Figure 5. Real-drifter-based correlation dimension at (top) 0.5, (middle) 1, and (bottom) 3 days, mapped to the initial (left)**

739 **and current (middle and right) positions of drifters.**

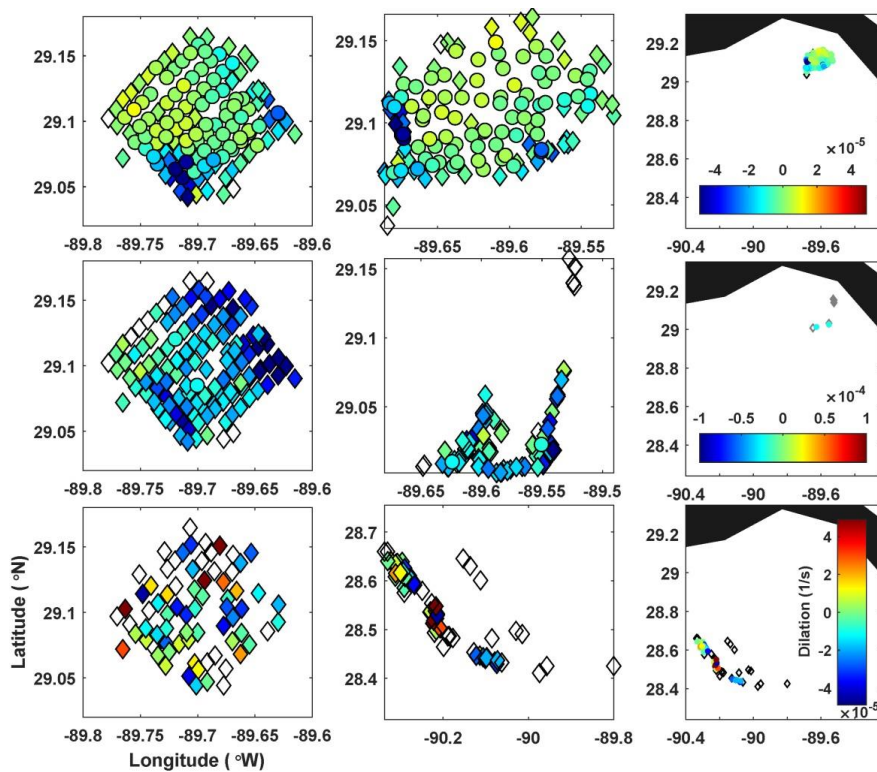
740



741

742 Figure 6. Real-drifter-based encounter volume at (top) 0.5, (middle) 1, and (bottom) 3 days, mapped to the initial (left) and

743 current (middle and right) positions of drifters.



744

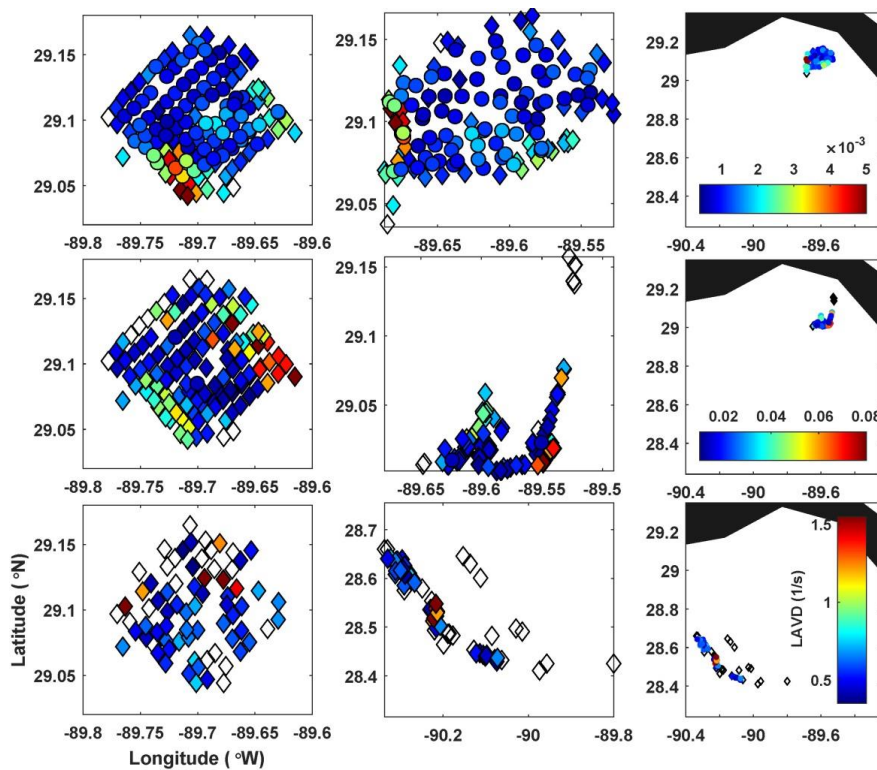
745 **Figure 7. Real-drifter-based dilation at (top) 0.5, (middle) 1, and (bottom) 3 days, mapped to the initial (left) and current**

746 **(middle and right) positions of drifters.**

747

748

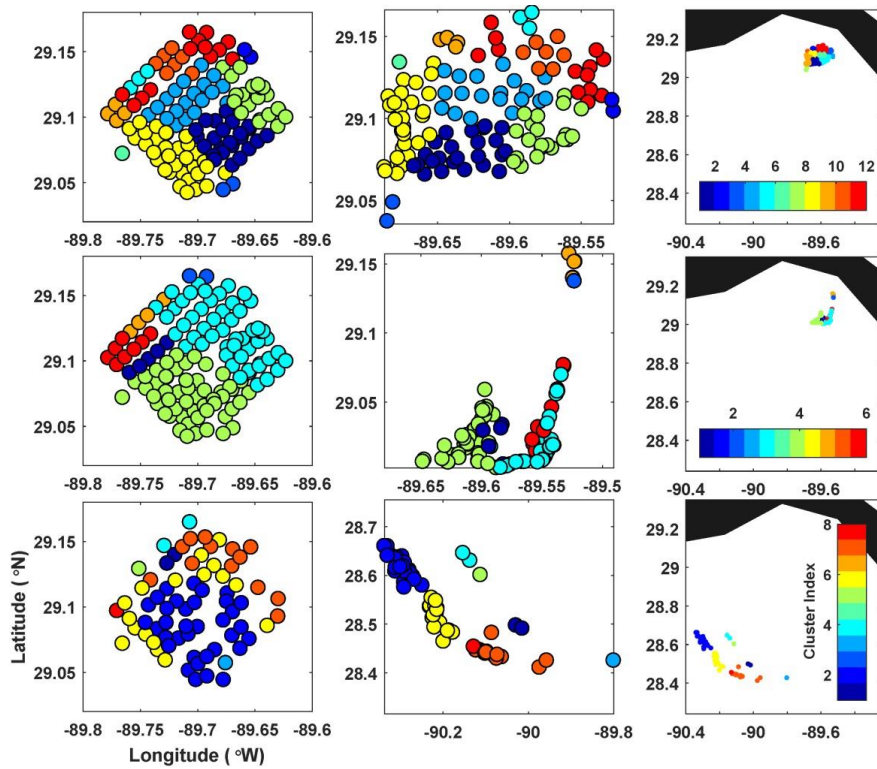




749

750 **Figure 8. Real-drifter-based LAVD at (top) 0.5, (middle) 1, and (bottom) 3 days, mapped to the initial (left) and current**

751 **(middle and right) positions of drifters.**



752

753 **Figure 9.** Real-drifter-based spectral clusters at (top) 0.5, (middle) 1, and (bottom) 3 days, mapped to the initial (left) and

754 current (middle and right) positions of drifters.

755

756

757

758

759

760